Multi-Objective Optimization of a Magnetically Levitated Planar Motor with Multi-Layer Windings

Liang Guo, He Zhang, *Member, IEEE,* Michael Galea, *Member, IEEE,* Jing Li, *Member, IEEE,*

and Chris Gerada, *Senior Member, IEEE*

*Abstract***—In this paper, a novel magnetically levitated coreless planar motor with three-layer orthogonal overlapping windings is shown to have higher power density and higher space utilization compared to other coreless planar motors. In order to achieve maximum forces with minimum cost and minimum space, a multi-objective optimization of the novel planar motor is carried out. In order to reduce the computational resources required for finite element analyses, a fast but accurate analytical tool is developed, based on expressions of the flux density of the permanent magnet array, which are derived from the scalar magnetic potential method. The validity and accuracy is verified by 3D FE results. Based on the force formulas and the multi-objective function derived from the analytical models, a particle swarm optimization (PSO) algorithm is applied to optimize the dimensions of the planar motor. The design and optimization of the planar motor is validated with experimental results, measured on a built prototype, thus proving the validity of the analytical tools.**

Liang Guo is with Faculty of Mechanical Engineering & Automation, Zhejiang Sci-Tech University, Hangzhou, 310018, CHINA(e-mail: lguo@ zstu.edu.cn).

He Zhang, Galea Michael, Jing Li and Christopher Gerada are with the Power Electronics, Machines and Control Group, Department of Electrical and Electronic Engineering, Faculty of Engineering, The University elf Nottingham, Nottingham, NG7 2RD, U.K. (e-mail: he. Zhang @nottingham.ac.uk; michael.galea@nottingham.ac.uk; jing.li@nottingham.ac.uk; chris.gerada @ nottingham.ac.uk).

He Zhang and Chris Gerada are also with The University of Nottingham, Ningbo, CHINA.

Index Terms—**Analytical modeling, planar motor, overlapping windings, multi-objective optimization,.**

I. INTRODUCTION

LINEAR actuation for industrial and mobile applications has seen considerable research effort in the last two decades, with significant improvements in terms of force density and thermal performances [1~5] being achieved. Closely related to the linear machine research field, considerable research on the development and use of magnetically levitated planar motors, especially permanent magnet (PM) planar motors, has also increased rapidly[6~11].Potential advantages of such motors include high power density, a simple structure[12~14], direct driving, low friction[15，16] and no backlash. This makes the PM planar potentially attractive for applications such as semiconductor lithography systems and other high-precision industrial applications, although its uptake is limited and published literature shows that the concept has not been taken to industrialization yet.

A novel magnetically levitated PM planar motor with multi-layer orthogonal overlapping windings was proposed in [17]. The structure of the planar motor is shown in Fig.1, where the two dimensional (2D) PM array is the stator, and the overlapping windings are the mover. The mover consists of two sets of x-direction windings and two sets of y-direction windings. The effective areas of both direction windings are equal to the full area of the mover section, which results in full utilization of space and magnetic field. By controlling the currents in the windings separately, the planar motor can achieve 5 degrees of freedom (DOF), due to the decoupled x and y axes forces. From the preliminary studies in [17], its potential, in terms of force density when compared to the two-layer windings topology used in [18], is highly promising mainly due to the enhanced material utilization.
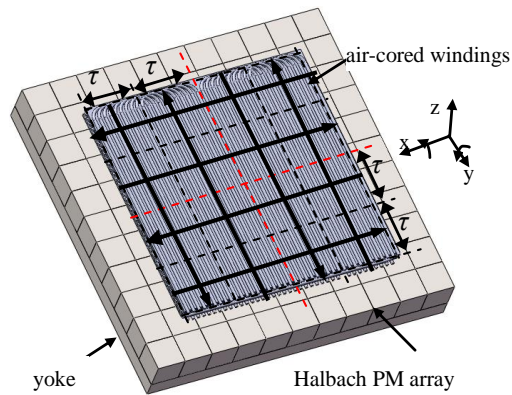
Fig.1. Topology of the planar motor.

A novel magnetically levitated PM planar motor with multi-layer orthogonal overlapping windings was proposed in [17]. The structure of the planar motor is shown in Fig.1, where the two dimensional (2D) PM array is the stator, and the overlapping windings are the mover. The mover consists of two sets of x-direction windings and two sets of y-direction windings. The effective areas of both direction windings are equal to the full area of the mover section, which results in full utilization of space and magnetic field. By controlling the currents in the windings separately, the planar motor can achieve 5 degrees of freedom (DOF), due to the decoupled x and y axes forces. From the preliminary studies in [17], its potential, in terms of force density when compared to the two-layer windings topology used in [18], is highly promising mainly due to the enhanced material utilization.

It is known that the finite element (FE) method is highly appropriate to calculate the magnetic field and performance of electrical machines [19]. However, FE analyses are in general very time consuming, especially when a large number of design iterations are required. This is more highlighted when the FE analysis in question involves 3D modeling. For a design problem such as that of the planar motor, it is therefore necessary to derive an accurate analytical model of the planar motor, which permits a high number of iterations at a much reduced cost in terms of computational time. This is especially valid for coreless machines such as the one under consideration.

Thus, in this paper, a multi-objective optimization, based on a particle swarm optimization (PSO) algorithm of the novel planar motor is proposed and thoroughly investigated. The PSO uses the analytical

model to determine the performance and subsequently find the optimal dimensions that result in the best force characteristics with minimum cost and maximum efficiency.

The advantages of the novel planar motor, such as the enhanced high force density and the higher space utilization, are then compared to those of other planar motors.

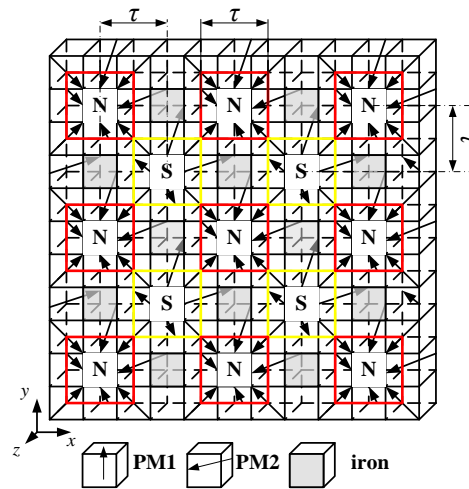## II. FIELD DISTRIBUTION DUE TO PERMANENT MAGNET

Fig.2. Permanent magnet array.

The 2D PM array used in the proposed planar motor is shown in Fig. 2, which is an innovative improvement on the structure proposed in [20]. For the PM array in [20], the remanence of PM2 is only $1/\sqrt{2}$ of the remanence of PM1. For Fig. 2, the PMs are all of one material with remanence Br=1.34T. The proposed array has N-pole modules and S-pole modules alternately distributed to increase the field density in the air-gap, in which the x-axis distances and y-axis distances between the PM poles are τ. Iron spacers are placed between the N and S modules in order to enhance the flux focusing capability. More details of the arrangement can be found in [17].

A. Analytical Modelling of the 2D PM Array

Since there is minimum magnetic saturation in the motor, the analytical solution for the magnetic field can be established based on the following assumptions:

1) The permeability of PMs is equal to that of air, i.e. relative permeability $\mu_r = 1$.

2) The effects of the iron spacers are neglected. The effects of eddy currents are also neglected.

3) The x and y-axes length of the PM array is infinite so that end-effects are neglected.

The scalar magnetic potential is used to solve the magnetic system. Since the material of the yoke in Fig.1 is aluminum, whose relative permeability is approximately 1, the field regions of the planar motor can then be assumed to be as shown in Fig. 3. Region I is the air/winding region above the PM array. Region II is the PM array region. Region III is the air/aluminum region below the PM array.
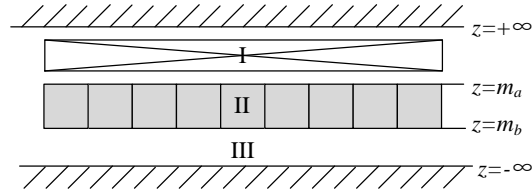

Fig.3. Field regions of planar motors.

Therefore, the scalar magnetic potential and the field vectors $\mathbf{B}$ and $\mathbf{H}$ in the air-gap/winding region (shown as I and III respectively) and the PM region(II) satisfy the following equations[6,11]:

1) In region I:

$$\nabla^2 \varphi_{\mathrm{I}} = 0, \mathbf{B}_{\mathrm{I}} = \mu_0 \mathbf{H}_{\mathrm{I}}, \mathbf{H}_{\mathrm{I}} = -\nabla \varphi_{\mathrm{I}} \qquad (1)$$

2) In region II:

$$\nabla^2 \varphi_{\mathrm{II}} = \nabla \cdot \mathbf{M}, \mathbf{B}_{\mathrm{II}} = \mu_0 \left(\mathbf{H}_{\mathrm{II}} + \mathbf{M} \right), \mathbf{H}_{\mathrm{II}} = -\nabla \varphi_{\mathrm{II}} \qquad (2)$$

3) In region III:

$$\nabla^2 \varphi_{\mathrm{III}} = 0, \mathbf{B}_{\mathrm{III}} = \mu_0 \mathbf{H}_{\mathrm{III}}, \mathbf{H}_{\mathrm{III}} = -\nabla \varphi_{\mathrm{III}} \qquad (3)$$

The boundary and interface conditions for the regions are as described in (4) and (5), where m_a and m_b are the z-axis position of the upper and lower surfaces of the PM array respectively.

$$\varphi_{\mathrm{I}} \big|_{z=+\infty} = 0, \varphi_{\mathrm{III}} \big|_{z=-\infty} = 0 \qquad (4)$$

$$
\begin{aligned}
H_{\mathrm{I}x} \big|_{z=m_a} &= H_{\mathrm{II}x} \big|_{z=m_a}, H_{\mathrm{II}x} \big|_{z=m_b} = H_{\mathrm{III}x} \big|_{z=m_b} \\
H_{\mathrm{I}y} \big|_{z=m_a} &= H_{\mathrm{II}y} \big|_{z=m_a}, H_{\mathrm{II}y} \big|_{z=m_b} = H_{\mathrm{III}y} \big|_{z=m_b} \qquad (5) \\
B_{\mathrm{I}z} \big|_{z=m_a} &= B_{\mathrm{II}z} \big|_{z=m_a}, B_{\mathrm{II}z} \big|_{z=m_b} = B_{\mathrm{III}z} \big|_{z=m_b}
\end{aligned}
$$

In the 2D PM array, the PM poles are magnetized in the z-direction, and the others are magnetized along the diagonal direction. As shown in Fig.4, by decomposing the residual magnetization vector into horizontal and vertical directions, the magnetic force of the PM array can be treated as a combination of the magnetic forces of three parts (Part 1, Part 2, Part 3) The equivalent residual magnetization of the PMs in Part 1 and Part 2 is $M/\sqrt{2}$. The equivalent residual magnetization of the PMs in Part 3 is $(1 - \sqrt{2})M$. The overall diagram of the analytical model of the new PM array is shown in Fig.5.
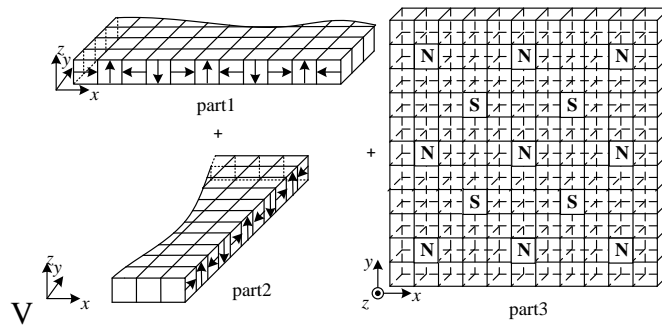

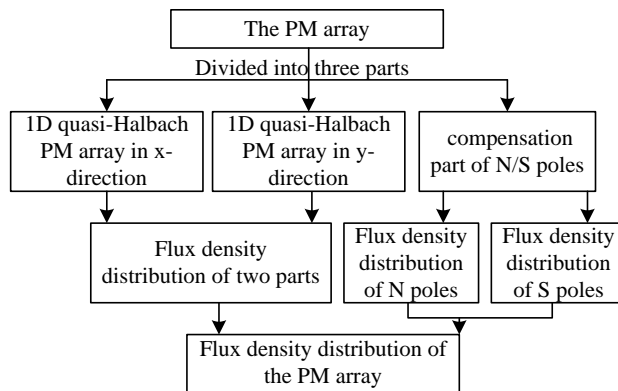Fig.4. Decomposition of the PM array.

Fig.5. Overall diagram of the analytical model.

a. Flux density of Part1 and Part2

It is clear that Part 1 and Part 2 are both 1D quasi-Halbach PM arrays. Assuming that the location of the origin is as shown in Fig.6, then the magnetization **M** in the two parts is as described in (6) and (7)[11].

Part 1: $\mathbf{M} = M_x\mathbf{e}_x + M_{zx}\mathbf{e}_z$ (6)

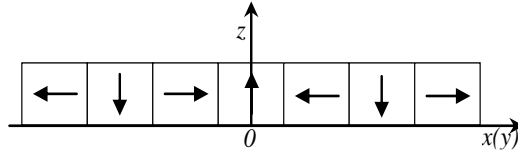Part 2: $\mathbf{M} = M_y\mathbf{e}_y + M_{zy}\mathbf{e}_z$ (7)

Fig.6. One dimension quasi-Halbach PM array.

The Fourier series of the magnetization vectors are given by (8) – (11)[11].

$$M_x = \frac{B_r}{\sqrt{2}\mu_0} \sum_{n=1,2,\cdots}^{\infty} a_n \cdot \cos(\frac{n\pi}{\tau} \cdot x) \tag{8}$$

$$M_{zx} = \frac{-B_r}{\sqrt{2}\mu_0} \sum_{n=1,2,\cdots}^{\infty} b_n \cdot \sin(\frac{n\pi}{\tau} \cdot x) \tag{9}$$

$$M_y = \frac{B_r}{\sqrt{2}\mu_0} \sum_{n=1,2,\cdots}^{\infty} a_n \cdot \cos(\frac{n\pi}{\tau} \cdot y) \tag{10}$$

$$M_{zy} = \frac{-B_r}{\sqrt{2}\mu_0} \sum_{n=1,2,\cdots}^{\infty} b_n \cdot \sin(\frac{n\pi}{\tau} \cdot y) \tag{11}$$

where $a_n = \frac{4}{n\pi} \cdot \sin\frac{n\pi}{2} \cdot \cos\frac{n\pi}{4}$, $b_n = \frac{4}{n\pi} \cdot \sin\frac{n\pi}{2} \cdot \sin\frac{n\pi}{4}$.

Thus, the general solutions of scalar magnetic potential in (1),(2) and (3) can be obtained by (12) – (14) where $K_2 = K_{21} \cdot e^{-\lambda_1 z} + K_{22} \cdot e^{\lambda_1 z}$.

$$\varphi_I = \sum_{n=1}^{\infty} K_1 \cdot e^{-\lambda_1 z} \cdot \left(\sin(\frac{n\pi x}{\tau}) + \sin(\frac{n\pi y}{\tau}) \right) \tag{12}$$

$$\varphi_{III} = \sum_{n=1}^{\infty} K_1 \cdot e^{-\lambda_1 z} \cdot \left(\sin(\frac{n\pi x}{\tau}) + \sin(\frac{n\pi y}{\tau}) \right) \tag{13}$$

$$\varphi_{II} = \sum_{n=1}^{\infty} \left(K_2 - \frac{B_r a_n \tau}{\mu_0 n\pi} \right) \cdot \left(\sin(\frac{n\pi x}{\tau}) + \sin(\frac{n\pi y}{\tau}) \right) \tag{14}$$

Combining the boundary conditions (4) and (5), the flux density distribution in the air-gap/winding (Section I) can be derived.

$$B_{Ix} = \mu_0 \sum_{n=1,2,\cdots}^{\infty} K_1 \cdot \lambda_1 \cdot e^{-\lambda_1 z} \cdot \cos(\frac{n\pi x}{\tau}) \tag{15}$$

$$B_{Iy} = \mu_0 \sum_{n=1,2,\cdots}^{\infty} K_1 \cdot \lambda_1 \cdot e^{-\lambda_1 z} \cdot \cos(\frac{n\pi y}{\tau}) \tag{16}$$

$$B_{Iz} = \mu_0 \sum_{n=1,2,\cdots}^{\infty} K_1 \cdot (-\lambda_1) \cdot e^{-\lambda_1 z} \cdot \left(\sin(\frac{n\pi x}{\tau}) + \sin(\frac{n\pi y}{\tau}) \right) \quad (17)$$

where: $\lambda_1 = \dfrac{n\pi}{\tau}$, $K_1 = (e^{\lambda_1 m_a} - e^{\lambda_1 m_b}) \cdot \dfrac{B_r}{2\sqrt{2}\lambda_1 \mu_0} \cdot (a_n + b_n)$.
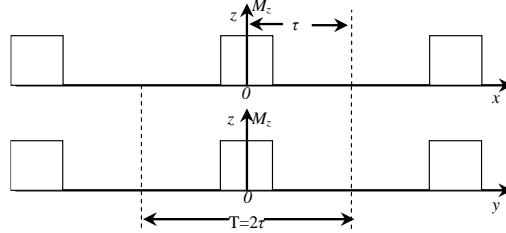
b. Flux density of Part3

Fig.7. Magnetization distribution of N poles.

In Fig.4, Part 3 is the compensation part of the array, which only consists of the N and S poles. The magnetization distribution of the N poles of Part 3 is shown in Fig.7. The Fourier series of these magnetization vectors are given by

$$M_z = M_0 (\frac{1}{4} + \sum_{n=1}^{\infty} a_n \cos\frac{n\pi x}{\tau})(\frac{1}{4} + \sum_{m=1}^{\infty} a_m \cos\frac{m\pi y}{\tau}) \qquad (18)$$

where: $M_0 = \dfrac{(1-\sqrt{2})B_r}{\mu_0}$, $a_i = \dfrac{2}{i\pi} \cdot \sin(\dfrac{i\pi}{4})$ $(i=n,m)$

The resolution of flux density distribution in the air-gap/winding section I due to the N poles can be derived as[21]:

$$B_{Ix} = \sum_{n=1}^{\infty}(-\lambda_2 K_{b1} e^{-\lambda_2 z} \sin\frac{n\pi x}{\tau} - \sum_{m=1}^{\infty} \lambda_2 K_{b3} e^{-\lambda_4 z} \sin\frac{n\pi x}{\tau}\cos\frac{m\pi y}{\tau}) \quad (19)$$

$$B_{Iy} = \sum_{m=1}^{\infty}(-\lambda_3 K_{b2} e^{-\lambda_3 z} \sin\frac{m\pi y}{\tau} - \sum_{n=1}^{\infty} \lambda_3 K_{b3} e^{-\lambda_4 z} \sin\frac{m\pi y}{\tau}\cos\frac{n\pi x}{\tau}) \quad (20)$$

$$B_{Iz} = K_{b0} + \sum_{n=1}^{\infty} -\lambda_2 K_{b1} e^{-\lambda_2 z} \cos\frac{n\pi x}{\tau} - \sum_{m=1}^{\infty} \lambda_3 K_{b2} e^{-\lambda_3 z} \cos\frac{m\pi y}{\tau} - \atop \sum_{n=1}^{\infty}\sum_{m=1}^{\infty} \lambda_4 K_{b3} e^{-\lambda_4 z} \cos\frac{n\pi x}{\tau}\cos\frac{m\pi y}{\tau} \qquad (21)$$

where: $\lambda_2 = \dfrac{n\pi}{\tau}$, $\lambda_3 = \dfrac{m\pi}{\tau}$, $\lambda_4 = \sqrt{\dfrac{(m^2+n^2)\pi^2}{\tau^2}}$ and

$$K_{b0} = \frac{(1-\sqrt{2})B_r}{16} \cdot e^{m_a} \cdot e^{-z},$$

$$K_{b1} = (e^{\lambda_2 m_b} - e^{\lambda_2 m_a}) \frac{(1-\sqrt{2})a_n B_r}{8\lambda_2},$$

$$K_{b2} = (e^{\lambda_3 m_b} - e^{\lambda_3 m_a}) \frac{(1-\sqrt{2})a_m B_r}{8\lambda_3},$$

$$K_{b3} = (e^{\lambda_4 m_b} - e^{\lambda_4 m_a}) \frac{(1-\sqrt{2})a_n a_m B_r}{2\lambda_4}$$

Considering the symmetry of the poles, based on the flux density expressions of the N poles (19) to (21), then the flux density distribution due to the S poles can be derived by assuming B_r of the S poles to be the inverse of the N poles. Thus B_r becomes $-B_r$ and similarly x becomes $(\tau+x)$ and y becomes $(\tau+y)$. Combining the flux density expressions of the N and S poles leads to the flux density expressions of Part 3.

c. Flux density of the PM array

Finally, by adding the expressions of the three parts up together, the flux density expressions of the 2D PM array can be obtained as shown below.

$$B_{Ix} = \sum_{n=1}^{\infty}(-\lambda_2 K_{b1}C_1 e^{-\lambda_2 z}\sin\frac{n\pi x}{\tau} - \sum_{m=1}^{\infty}\lambda_2 K_{b3}C_3 e^{-\lambda_4 z}\sin\frac{n\pi x}{\tau}\cos\frac{m\pi y}{\tau}) \quad (22)$$

$$B_{Iy} = \sum_{m=1}^{\infty}(-\lambda_3 K_{b2}C_2 e^{-\lambda_3 z}\sin\frac{m\pi y}{\tau} - \sum_{n=1}^{\infty}\lambda_3 K_{b3}C_3 e^{-\lambda_4 z}\sin\frac{m\pi y}{\tau}\cos\frac{n\pi x}{\tau}) \quad (23)$$

$$B_{Iz} = \sum_{n=1}^{\infty}-\lambda_2 K_{b1}C_1 e^{-\lambda_2 z}\cos\frac{n\pi x}{\tau} - \sum_{m=1}^{\infty}\lambda_3 K_{b2}e^{-\lambda_3 z}C_2\cos\frac{m\pi y}{\tau} -$$
$$\sum_{n=1}^{\infty}\sum_{m=1}^{\infty}\lambda_4 K_{b3}C_3 e^{-\lambda_4 z}\cos\frac{n\pi x}{\tau}\cos\frac{m\pi y}{\tau} \quad (24)$$

where $C_1 = 1-\cos(n\pi)$, $C_2 = 1-\cos(m\pi)$,

$C_3 = 1-\cos(n\pi)\cos(m\pi)$

B. Comparison with 3D Finite Element Model

In order to validate the analytical model presented above, then a 3D FE model of the PM array is also built. The main parameters of the 2D PM array are given in Table. I.

Fig.8 shows the air-gap flux density distributions of the proposed magnet array in the *x-y* plane. Fig. 7(a)

is the flux density calculated by the analytical model, while Fig. 7(b) is the flux density calculated by the 3D

FE model. This accounts for the end-effects and the magnetic non-linearity of the iron spacers.   The

analytical model results are very similar to those of the FE model in the central area of the machine. Toward

the end parts of the machine the FE results are slightly lower than those of the analytical model.   The

difference of the peak values between the two methods is about 0.034 T, which is approximately 5% of the

peak value. This is due to the reasons mentioned above.
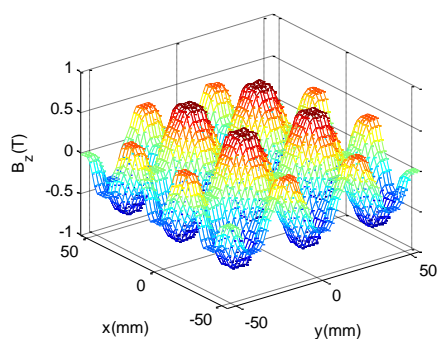
(a)
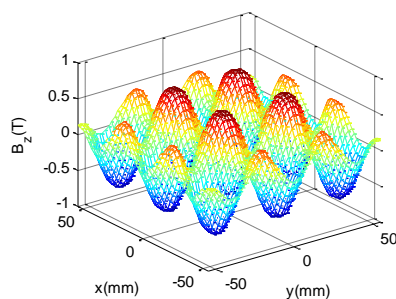
(b)

Fig.8. Air-gap flux density distribution. (a) Analytical result. (b) FE result.

TABLE I

PARAMETERS OF THE PM ARRAY

Item	Symbol	Value
Poles number of PM	P	13

arrays			
Pole pitch		T	$20mm$
Thickness of PM		h_m	$10mm$
The remanence of PM		B_r	1.32T
The relative permeability of PM		μ_r	1.2

Considering that the length of the windings is a multiple of 2τ, to uncouple the thrusts between the x-axis and y-axis, (according to the symmetric nature of the PM array), (25) and (26) can be identified.

$$B_{zav\_y} = \frac{1}{2\tau}\int_{-\tau}^{\tau} B_z dy, \ B_{zav\_x} = \frac{1}{2\tau}\int_{-\tau}^{\tau} B_z dx \qquad (25)$$

$$B_{xav} = \frac{1}{2\tau}\int_{-\tau}^{\tau} B_x dy, \ B_{yav} = \frac{1}{2\tau}\int_{-\tau}^{\tau} B_y dx \qquad (26)$$

Quantifiable measure of the characteristics of the PM array and its influence on the performances of the motor can be achieved by considering the average values of the expressions above.

Fig. 9 shows the variation of the fundamental wave amplitude of the B_{zav} relative to the height of air-gap, in which, the model 1 analytical curve represents the results of the new array calculated by analytical method, the model 1 FEM curve represents the results of the new array calculated by FEM and the model 2 FEM curve represents the results of the PM array reported in [20] calculated by FEM. It can be found that the results of analytical method are in good agreement with those of the 3D FEM. The fundamental amplitude of the flux density generated by the new array is more than 30% higher than the flux density generated by the PM array reported in [20] based on the same dimensions and same PM1 materials as shown in Fig.2. The space utilization is improved and as shown in Fig.10, the harmonic presence in the new configuration is also decreased, especially the 3rd harmonic, which is about 33% lower than that of the array reported in [20]. The ignoring of the iron spacers and the permeability of the PMs cause the relatively large harmonic in the analytical model compared to the FEM models.
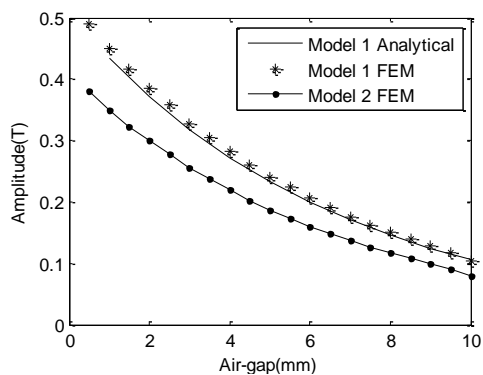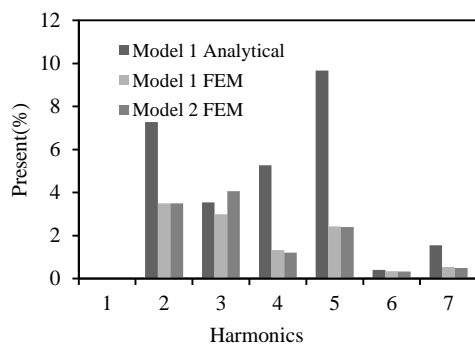
Fig.9. Amplitude of fundamental wave in $B_{zav.}$

Fig.10. Comparison of the harmonics in B_{zav}(airgap=2mm).

III. EMF AND FORCE CALCULATION

Based on the flux density distribution, the equations of the back-EMF and the forces for the proposed motor can also be derived. The equations help to evaluate the performance of the motor and can be used to achieve an optimized design and an improved control system.

In order to achieve higher force density values and higher material utilization, a three layer winding topology is adopted in the planar motor. In the topology, the first and third layers windings are both configured for the same direction, which are connected in series and both have a thickness h_{c1}. The windings in the secondary layer make up the other direction and have a thickness of $2h_{c1}$. The main dimensions of the windings are shown in Fig.11 and Table.II. When the number of pole pairs of the planar motor is 2, the number of the windings in x(y)-direction is 6.
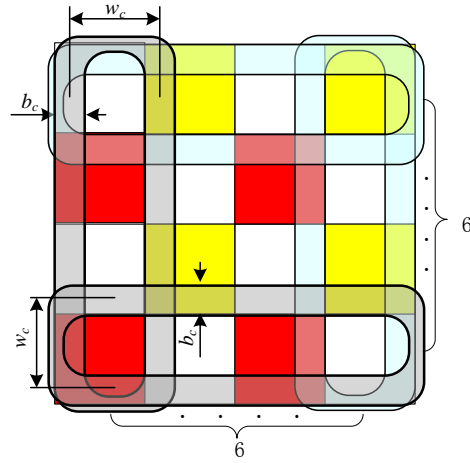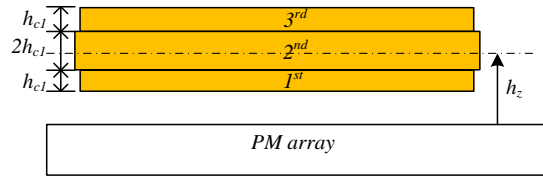
Fig.11. Diagram of the windings.

Fig. 12. Distribution of three-layer windings.

A. Electromotive Force Calculation

With a three-layer windings topology as shown in Fig.11 and Fig.12, the coil flux-linkage in the y-direction windings ϕ_y and x-direction windings ϕ_x can be calculated by the following integrations, where p is the number of pole pairs of the x-direction or the y-direction windings.

$$\phi_y = 2p\int_{-\frac{L}{2}}^{\frac{L}{2}}\int_{x-\frac{w_c}{2}}^{x+\frac{w_c}{2}}\left(\int_{h_z-2h_{c1}}^{h_z-h_{c1}}B_z dzdxdy+\int_{h_z+h_{c1}}^{h_z+2h_{c1}}B_z dzdxdy\right) \quad (27)$$

$$\phi_x = 2p\int_{-\frac{L}{2}}^{\frac{L}{2}}\int_{y-\frac{w_c}{2}}^{y+\frac{w_c}{2}}\int_{h_z-h_{c1}}^{h_z+h_{c1}}B_z dzdydx \quad (28)$$

Considering the length of the windings is a multiple of period of $B_z(2\tau)$, then as to (25), the forces equation can be re-written as shown in (29, 30).

$$\phi_y = 2pL\int_{x-\frac{w_c}{2}}^{x+\frac{w_c}{2}}\left(\int_{h_z-2h_{c1}}^{h_z-h_{c1}}B_{zav\_y}dzdx+\int_{h_z+h_{c1}}^{h_z+2h_{c1}}B_{zav\_y}dzdx\right) \quad (29)$$

$$\phi_x = 2pL\int_{y-\frac{w_c}{2}}^{y+\frac{w_c}{2}}\int_{h_z-h_{c1}}^{h_z+h_{c1}}B_{zav\_x}dzdy \quad (30)$$

Since the harmonic presence is smaller than 4%, the harmonics of the air-gap flux density can safely be ignored.

$$B_{zav\_y} = B_{zm}\cos(x), \; B_{zav\_x} = B_{zm}\cos(y) \qquad (31)$$

Hence, the inducted EMF per phase can be simplified as:

$$e_y = -N\frac{d\phi_y}{dt} = 8ph_{c1}LB_{z1}K\sin(\frac{x\pi}{\tau})v \qquad (32)$$

$$e_x = -N\frac{d\phi_x}{dt} = 8ph_{c1}LB_{z2}K\sin(\frac{y\pi}{\tau})v \qquad (33)$$

where, N is the turns of the winding per phase, v is the linear velocity, $K = \sin(\frac{b_c\pi}{2\tau})\sin(\frac{w_c\pi}{2\tau})$,

$$B_{z2} = \frac{1}{2h_{c1}}\int_{h_z-h_{c1}}^{h_z+h_{c1}} B_{zm}dz \text{ and}$$

$$B_{z1} = \frac{1}{2h_{c1}}\left(\int_{h_z-2h_{c1}}^{h_z-h_{c1}} B_{zm}dz + \int_{h_z+h_{c1}}^{h_z+2h_{c1}} B_{zm}dz\right).$$

B. Electromagnetic Force Calculation

For a three-layer winding topology, considering the equation $F = \int_v (J \times B)dv$, the Lorentz force generated in one set of y-direction windings can be expressed as:

Thrust force:

$$F_x = 2p\int_{-\frac{L}{2}}^{\frac{L}{2}}\int_{x-\frac{w_c}{2}}^{x+\frac{w_c}{2}}\left(\int_{h_z-2h_{c1}}^{h_z-h_{c1}} J_yB_zdzdxdy + \int_{h_z+h_{c1}}^{h_z+2h_{c1}} J_yB_zdzdxdy\right)(34)$$

Normal force:

$$F_{z1} = 2p\int_{-\frac{L}{2}}^{\frac{L}{2}}\int_{x-\frac{w_c}{2}}^{x+\frac{w_c}{2}}\left(\int_{h_z-2h_{c1}}^{h_z-h_{c1}} J_yB_xdzdxdy + \int_{h_z+h_{c1}}^{h_z+2h_{c1}} J_yB_xdzdxdy\right) \quad (35)$$

Therefore, the force generated in one set of the x-direction windings can be expressed as

Thrust force: $\; F_y = 2p\int_{-\frac{L}{2}}^{\frac{L}{2}}\int_{y-\frac{w_c}{2}}^{y+\frac{w_c}{2}}\int_{h_z-h_{c1}}^{h_z+h_{c1}} J_xB_zdzdydx \qquad (36)$

Normal force: $\; F_{z2} = 2p\int_{-\frac{L}{2}}^{\frac{L}{2}}\int_{y-\frac{w_c}{2}}^{y+\frac{w_c}{2}}\int_{h_z-h_{c1}}^{h_z+h_{c1}} J_xB_ydzdydx \qquad (37)$

By considering

$$B_{xav} = B_{xm} \sin(x), \ B_{yav} = B_{ym} \sin(y) \tag{38}$$

$$B_{y1} = \frac{1}{2h_{c1}} \int_{h_z - h_{c1}}^{h_z + h_{c1}} B_{ym} dz \tag{39}$$

$$B_{x1} = \frac{1}{2h_{c1}} \left(\int_{h_z - 2h_{c1}}^{h_z - h_{c1}} B_{xm} dz + \int_{h_z + h_{c1}}^{h_z + 2h_{c1}} B_{xm} dz \right) \tag{40}$$

Then $(34 - 37)$ can be simplified as described by $(41) - (44)$, where θ_x and θ_y are the electrical angle between the current synthetic vector of the y-direction windings and x-direction windings with their d-axis respectively.

$$F_x = \frac{12 p h_{c1} \tau L B_{z1} J_y}{\pi} K \sin(\theta_x) \tag{41}$$

$$F_y = \frac{12 p h_{c1} \tau L B_{z2} J_x}{\pi} K \sin(\theta_y) \tag{42}$$

$$F_{z1} = \frac{12 p h_{c1} \tau L B_{x1} J_y}{\pi} K \cos(\theta_x) \tag{43}$$

$$F_{z2} = \frac{12 p h_{c1} \tau L B_{y1} J_x}{\pi} K \cos(\theta_y) \tag{44}$$

C. Comparison of Force Characteristics

In order to identify the advantages of the proposed novel winding topology, its force characteristics is compared to those of two typical winding topologies (Fig.13). The topology in Fig.13(a) is presented in [22], where the concentric windings also consist of the x-direction windings and the y-direction windings, however the effective area of one direction windings is only ½ that of the mover surface. The latter one is presented in [23],where the windings consist of nine-phase windings. The advantage of the topology is that all the windings can generate x and y direction forces. Similar to the novel overlapping winding topology, almost100% of the mover surface in [23] is used to generate the one-direction thrust.

Table II compares the force characteristics of the three different winding topologies, such as the maximum thrust force, utilization of the copper and the force density. According to the results, it can be found that the

proposed, novel motor has the highest force density D and can provide the highest force C with same copper
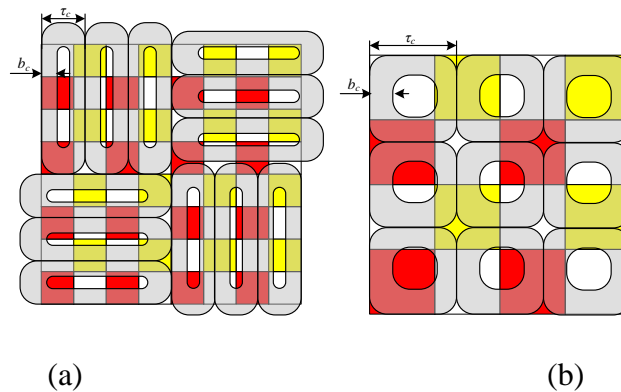
loss. However the DOF is lower than the motor in [22].

(a)   (b)

Fig.13. Winding topology of (a) Compter [22], (b) Kou [23].

TABLE II

DIMENSION PARAMETERS OF THE WINDINGS

Winding Topology	Proposed	Compter [20]	Kou[21]
Degree of Freedom	5	6	3
Number of pole pairs of the whole windings p	4	4	4
Coil pitch τ_c	$4\tau/3$	$4\tau/3$	$4\tau/3$
Bundle width b_c	$\tau/3$	$0.55\,\tau$	$1.4\tau/3$
Coil width w_c	τ	$0.783\,\tau$	$2.6\tau/3$
Coil effective length	$8\,\tau$	$4\,\tau$	$2.6\tau/3$
Number of coils	24	12	36

Thickness of one-direction coil	$h_c/2$	h_c	h_c
Minimum Mover size S	$8.33\tau*8.33\ \tau$	$8.55\tau*8.55\tau$	$8\tau*8\tau$
Maximum Thrust F	$15.287B_z h_c J\tau^2$	$10.92B_z h_c J\tau^2$	$13B_z h_c J\tau^2$
Copper loss P_{loss}	$36h_c \tau^2 \rho J^2$	$31.57h_c \tau^2 \rho J^2$	$58.24h_c \tau^2 \rho J^2$
$C=\dfrac{F}{P_{loss}}$	$0.425B_z/J\rho$	$0.346B_z J$	$0.223B_z J$
$D=\dfrac{F}{S}$	$0.220B_z h_c J$	$0.149B_z h_c J$	$0.203B_z h_c J$

IV. OPTIMIZATION OF THE PLANAR MOTOR

A. Objective Function

In this paper, the objective is to maximize the output force of the planar motor for the same current density while minimizing the cost and maximizing the efficiency. Since the side lengths of the sides of the magnet cube in the array are all equal to $\tau/2$, the height of the PM is determined with a certain τ. The main dimensions need to be optimized in the planar motor are the pole pith of the magnet array τ, the length of the windings L and the height of the windings h_c.

According to the analytical model of the PM array(15)~(17) and (22)~(24), the flux density decreases exponentially with the height of air-gap. For the fundamental, the exponential factor is $-\pi/\tau$. The attenuation of the flux density is lowered with the increment of τ. It means that a higher electromagnetic force will be generated with bigger pole pitch τ with fixed length L. But at the same time, the increment of τ will enhance the height of the PM array $\tau/2$ and the bundle width of the windings $\tau/3$. The volume of the PM array and the volume of the end-part windings also will be increased. Therefore, there is a tradeoff between the forces and the space and cost of the PM.

With the fixed winding length L and the fixed pole pitch τ, the increment of the height of the windings h_c will enhance the forces, at the cost of weight. This indicates that to achieve the highest levitation force possible an optimal value of h_c exists.

There are numerous methods for multi-objective optimization. One of the most adopted ones is to aggregate all objective functions to create a composite single-objective function to minimize and then use optimization algorithms to obtain an optimal solution. According to the optimization goal, the objective function is defined as

$$OF = \frac{-F_L}{V_m \cdot P_{loss}} \tag{45}$$

where F_L is the parameter to represent the force characteristic of the motor, which is set such that $F_L = F_{Lmean} + F_{Lgm}$. F_{Lmean} is the mean value of the levitation force in the entire suspension stroke, F_{Lgm} is the value of the levitation force with the mover in the middle of the suspension stroke. V_m is the volume of the PM array in the planar motor, which determines the space and the cost of the planar motor. P_{loss} is the loss of the planar motor, $P_{loss} = \sum_{i=1}^{4} I_i^2 R_i$, where i is the number of the windings, which determines the efficiency of the planar motor.

To get an eligible solution, some constraints are involved during the optimization. These are:

$$\begin{cases} p = 2n \ (n \geq 1) \\ F_{L\max} \geq F_{set} \end{cases} \tag{46}$$

where $F_{L\max}$ is the maximum of the levitation force, which should be bigger than the required force F_{set}. Since the pole pairs of each set of windings is an integer n, the total p of the windings should be $2n$.

B. PSO optimization

The PSO is a population-based stochastic optimization algorithms inspired by the social behavior of flocking organisms, such as swarms of honeybees and fish shoals. It uses a population of individuals (particles) to probe and assess promising regions of the search space. In the movement, each particle memories the best position it ever encountered and the moving velocity is dynamically adjusted according to

the relationship between its previous best position and the best position ever attained by all particles. Therefore, the particles have the tendency to move toward the increasingly better search area over the whole course of the search process [24~28].

When there are k dimensions to be optimized the PSO algorithm starts with N sets of k-dimensional particles randomly scattered over a k-dimensional searching space. The ith particle can be represented by a k-dimensional vector,

$$X_i = [x_{i1}, x_{i2}, \cdots, x_{ik}]^T$$

The velocity of the ith particle is also a k-dimension vector:

$$V_i = [v_{i1}, v_{i2}, \cdots, v_{ik}]^T$$

The best position that is encountered by the ith particle, i.e. the existing minimum value of the ith particle in the objective function, is:

$$P_i = [p_{i1}, p_{i2}, \cdots, p_{ik}]^T$$

The best position in P_1~P_N is

$$P_g = [p_{g1}, p_{g2}, \cdots, p_{gk}]^T$$

When the N sets of particles are searching for the optimum, the particles update their velocities according to the best positions at each generation. For the $s+1$ generation, the velocity of the ith particle should be[28]:

$$\begin{aligned} v_{id}(s+1) = & \omega v_{id}(s) + C_1 r_1 (P_{id}(s) - x_{id}(s)) \\ & + C_2 r_2 (P_{gd}(s) - x_{id}(s)) \end{aligned} \qquad (47)$$

$$x_{id}(s+1) = x_{id}(s) + \chi v_{id}(s+1) \qquad (48)$$

Where ω is the inertia, χ is constriction factor, C_1 and C_2 denote the cognitive and social parameters, r_1 and r_2 are random numbers uniformly distributed in the interval [0,1].

C. *Optimization Results*

A preliminary analytical design exercise was done in order to identify an appropriate starting value for N. Thus, for the optimization of the planar motor, initially N in the PSO is set to be 30, k is set to be 3, the inertia ω is set to be 0.7298, the cognitive and social parameters C_1 and C_2 are set to be 1.4962 and the constriction

factor χ is set to be 1. The three dimensions of the particles correspond to the main three dimensions of the planar motor, i.e. the pole pitch τ, the length of the windings L and the thickness of the windings h_{c1}. When the required force F_{set} is set to be 10N, the levitation stroke is from 2mm to 6mm. With these specifications, the evolution algorithm is completed after 48 iterations with the objective function as shown in (45).

The variation of the fitness is shown in Fig.14. The corresponding positions of the particles, the variation of three dimensions, are shown in Fig.15. It is clear that the PSO has an excellent convergence rate. The particles flock together towards the best position within 25 iterations. The optimal dimensions are thus found to be $\tau=9.975mm$, $L=79.8mm$, $h_{c1}=1.18mm$.

When the required force F_{set} is set to be 1000N, the levitation stoke is from 3mm to 9mm. For these conditions the evolution is completed after 60 iterations, relative to the objective function shown in (45). The optimization dimensions are $\tau=52.06mm$, $L=416.5mm$, $h_{c1}=3.8mm$.
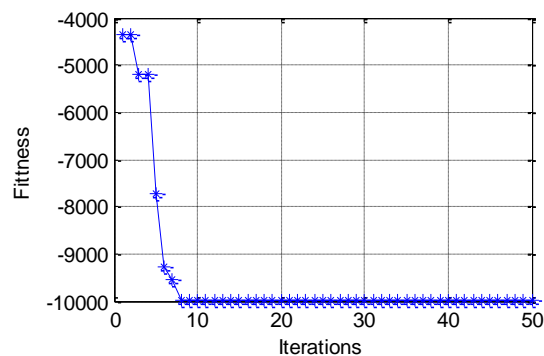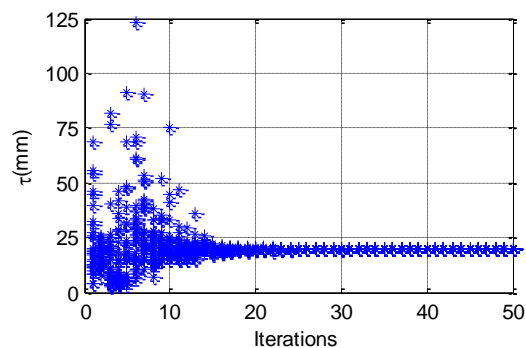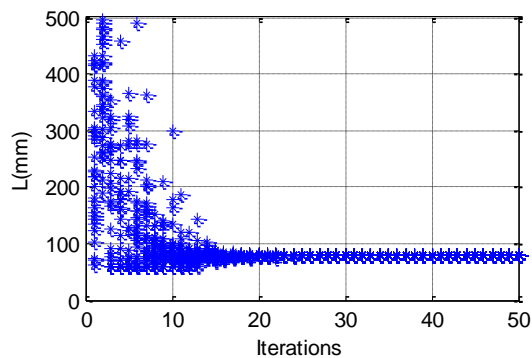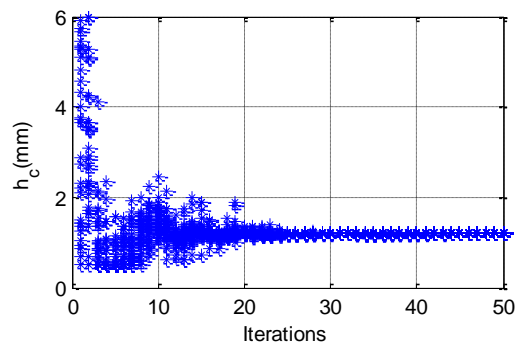

Fig.14. The variation of the fitness.

(a)

(b)

(c)

Fig.15. The positions of the particles. (a) Pole pitch. (b) Length of the windings. (c) Thickness of the windings.

V. SIMULATION AND EXPERIMENT

Based on the optimized results presented above, a prototype of the three-layer planar motor with dimensions τ=10mm, L=80mm, h_{c1}=1mm has been manufactured. The prototype and the experiment system are shown in Fig.16.

By using a gauss meter, the flux density distribution in the plane with g=2mm is measured, which is shown in Fig.17(a). Fig.17(b) is the difference between the flux density results obtained by experimental measurements and the analytical method where the mean difference is smaller than 0.03T. The results of the analytical method are in good agreement with the experimental results. The high difference near the edges is because end-effects are not considered in the analytical method. However when the range of the mover's motion isn't bigger than the PM area, the influence of the end-effect can safely be ignored.
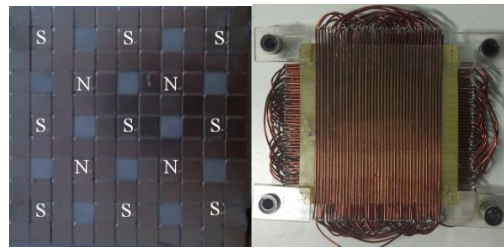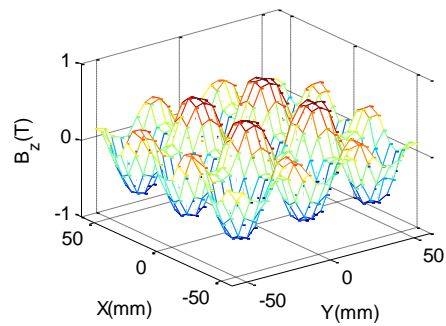
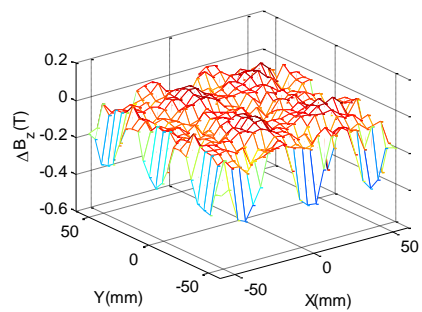(a)   (b)
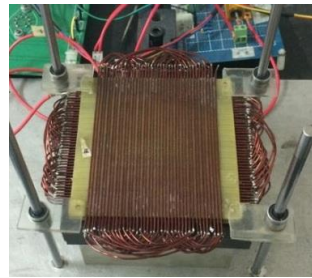
(c)

Fig.16. The prototype of the planar motor.(a) Permanent magnet array. (b) Multi-layer Windings. (c) Experiment system.

(a)

(b)

Fig.17. Experimental results of air-gap flux density distribution. (a) Measurement result. (b) Difference between the results of two methods.

Four linear guides are placed on the angles of the resin board to provide an improved translational accuracy. The relationship between the levitation height and windings current is shown in Fig.18. When the levitation height is 5mm and the movers is driven in x-direction with a velocity of 0.17m/s, the back-EMF curve generated in one turn of y-direction windings is shown in Fig.19. In Fig.18 and Fig.19, the simulation results are derived from the 3D FEM results. The similarity between the experimental and the FE results indicate the validity of the analytical models. Because of the slight fluctuation of the velocity in the experiment, the measured back-EMF curve is not as smooth as the analytical results. The amplitude of the measured back-EMF is $8.18mV$ and the amplitude of the EMF calculated by the analytical method is $8.1mV$. The difference between the results is only 1%.
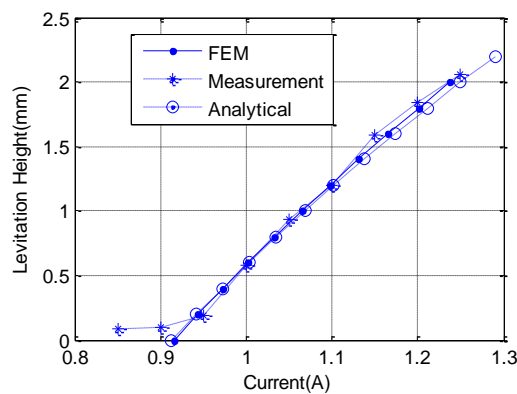

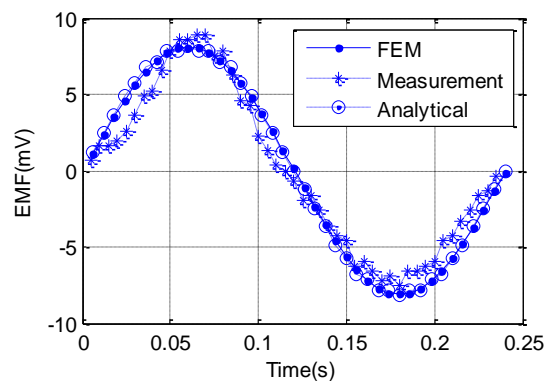Fig.18. Relationship between levitation height and current.

Fig. 19. EMF curves.

VI. CONCLUSION

In this paper, a multi-objective optimization of a planar motor with three-layer overlapped windings has been proposed with the main objective of achieving maximum force density with minimum cost. Instead of 3D FE analysis, the optimization of the planar motor is based on the analytical expressions of the flux density of the PM array and the formulas of forces. According to the dynamic process of the optimization based on the PSO algorithm, the proposed multi-objective optimization method is shown to be timesaving and to have the capability to find the best results with quick convergence.

By comparing with other planar motors, the advantages of this novel planar motor, such as high force density and high space utilization have been validated. The flux density generated by the improved PM array is 33% higher than that of the original one. The force density of the novel winding topology is 22.5% higher than that of other two classic winding topologies. An important conclusion from this work is the exponential damping relationship between the flux density and the height of air-gap that was identified and validated by experimental results.

A fast but accurate analytical tool for design and optimization of planar motors has been developed, based on expressions of the flux density of the PM array. Its accuracy has been validated by the FE results and also by the experiment results of the prototype. This tool will serve to facilitate future work regarding such planar motors.

As future work, intelligent, nonlinear control strategies based on the analytical model will be further investigated to realize improved high-precision control and positioning.

REFERENCES

[1] M. Galea, G. Buticchi, L. Empringham, L. De Lillo, and C. Gerada, "Design of a High-Force-Density Tubular Motor," *IEEE Trans. Ind. Appl.*, vol. 50, pp. 2523-2532, Jul. 2014.

[2] M. Galea, C. Gerada, T. Raminosoa, and P. Wheeler, "A Thermal Improvement Technique for the Phase Windings of Electrical Machines," *IEEE Trans. Ind. Appl.,* vol. 48, pp. 79-87, Jan. 2012.

[3] L. Cappelli, Y. Coia, F. Marignetti, Z.Q. Zhu, "Analysis of eccentricity in permanent-magnet tubular machines," *IEEE Trans. Ind. Electron.*, vol. 61,No.5, pp. 2208-2216, May 2014.

[4] I.C. Vese, F. Marignetti and M. M. Radulescu, "Multiphysics approach to numerical modeling of a permanent-magnet tubular linear motor," *IEEE Trans. Ind. Electron.*, vol. 57,No.1, pp. 320-326, Jan.2010.

[5] L. Guo, H. Zhang, J. Li, M. Galea, and C. Gerada "Analysis and optimization of a double-sided, air-cored tubular generator", *IEEE Trans. Magn.*. vol. 51,No.11,8206904, Nov. 2015.

[6] H. Cho, C. Im and H. Jung, "Analysis and design of synchronous permanent-magnet planar motor," *IEEE Trans. Energy Convers.,* Vol.17, No.4, pp:492-499, Dec. 2002.

[7] H. Zhang, B. Kou, H. Zhang and Y. Jin. "A three-degree-of-freedom short-stroke lorentz-force-driven planar motor using a halbach permanent-magnet array with unequal thickness," *IEEE Trans. Ind. Electron.*, vol. 62,No.6, pp. 3640-3650, Jun. 2015.

[8] M. Y. Chen, T. B. Lin, S. K. Hung, and L. C. Fu, "Design and experimentof a macro-micro planar maglev positioning system," *IEEE Trans. Ind. Electron.*, vol. 59, no. 11, pp. 4128–4139,Nov. 2012.

[9] J. Choi, J. Park, and Y.Baek, "Design and experimental validation of performance for a maglev moving-magnet-type synchronous PM planar motor," *IEEE Trans. Magn.,* Vol.42, No.10, pp:3419-3421,Oct.2006.

[10]J.M.M. Rovers, J.W.Jansen, J.C. Comper and E. A. Lomonova, "Analysis method of the dynamic force and torque distribution in the magnet array of a commutated magnetically levitation planar actuator," *IEEE Trans. Ind. Electron.*, Vol.59, No.5, pp:2157-2166, May 2012.

[11]V. Nguyen, W. Kim, "Novel Electromagnetic design for a precision planar positioned moving over a superimposed concentrated-field magnet matrix," *IEEE Trans. Energy Convers.,* Vol.27, No.1, pp:52-62, Mar. 2013.

[12] O.-S. Kim, S.-H. Lee, and D.-C. Han, "Positioning performance and straightness error compensation of the magnetic levitation stage supported by the linear magnetic bearing," *IEEE Trans. Ind. Electron.*, vol. 50, no. 2,pp. 374–378, Apr. 2003.

[13] M.-Y. Chen, H.-H. Huang, and S.-K. Hung, "A new design of a submicropositioner utilizing electromagnetic actuators and flexure mechanism," *IEEE Trans. Ind. Electron.*, vol. 57, no. 1, pp. 96–106, Jan. 2010.

[14] Z. Liu, F. Luo, and M. A. Rahman, "Robust and precision motion control system of linear-motor direct drive for high-speed X-Y table positioning mechanism," *IEEE Trans. Ind. Electron.*, vol. 52, no. 5, pp.357–1363, Oct. 2005.

[15] J. Pan, N. Cheung, and J. Yang, "High-precision position control of a novel planar switched reluctance motor," *IEEE Trans. Ind. Electron.*, vol. 52, no. 6, pp.1644–1652, Dec. 2005.

[16] J. Cao, Y.Zhu, J. Wang, W.Yin and G. Duan, "A novel synchronous permanent magnet planar motor and its model for control application," *IEEE Trans. Magn.*, vol. 41, no. 6, pp.2156–2163, Jun. 2005.

[17] L. Guo, H. Zhang, M. Galea, J. Li, W. Lu and C. Gerada "Analysis and Design of a Magnetically Levitated Planar Motor with Novel Multi-Layer Windings", *IEEE Trans. Magn.* vol. 51, no. 8, 8106909, Aug. 2015.

[18] Y.Ueda, H. Ohsaki, "A planar actuator with a small mover traveling over large yaw and translational displacements," *IEEE Trans. Magn.,* Vol.44, No.5, pp:609-616, May 2008.

[19] X. Zhang , W. Li, B. Kou, J. Cao, H. Cao, C. Gerada, H .Zhang, "Electro-thermal combined optimization on notch in air cooled High Speed Permanent Magnetic Generator", *IEEE Trans. Magn.* 8200210, Jan. 2015.

[20] D.L. Trumper, W. J. Kim, and M. E. Williams, "Magnetic arrays," *U.S.Patent* 5631618, May 1997.

[21] J. Boeij, E. Lomonova and A. Vandenput, "Modeling ironless permanent magnet planar actuator ,"*IEEE Trans. Magn.,* Vol.42, No.8, pp:2009-2016, Aug. 2006.

[22]J. C. Compter, "Electro-dynamic planar motor," *Precision Engineering*, vol. 28, no. 2, pp. 171–180, Apr. 2004.

[23]L. Zhang, B. Kou, L. Li, B. Zhao, "Characteristic analysis of a long-stroke synchronous permanent magnet planar motor". *IEEE Trans. Magn.,* Vol.48, No.11, pp:4658-4661, Nov. 2012.

[24]H. M. Hasnien, "Particle swarm design optimization of transverse flux linear motor for weight reduction and improvement of thrust force," *IEEE Trans. Ind. Electron.*, vol. 58, no. 11, pp. 4048–4056,Sep. 2011.

[25]N. Bracikowski, M. Hecquet, P. Brochet and S. V. Shirinskii, "Multiphysics modelling of a permanent magnet synchronous machine by using lumped models," *IEEE Trans. Ind. Electron.*, vol. 59, no. 6, pp. 2426–2437,Jun. 2012.

[26]C.-H. Liu and Y.-Y. Hsu, "Design of a self-tuning PI controller for a STATCOM using particle swarm optimization," *IEEE Trans. Ind. Electron.*, vol. 57, no. 2, pp. 702–715, Feb. 2010.

[27]Y.-X. Liao, J.-H. She, and M. Wu, "Integrated hybrid-PSO and fuzzy-NN decoupling control for temperature for reheating furnace," *IEEE Trans. Ind. Electron.*, vol. 56, no. 7, pp. 2704–2714, Jul. 2009.

[28]K. E. Parsopoulos, M. N. Vrahatis, "On the computation of all global minimizers through particle swarm optimization," *IEEE Trans. Evol. Compt.,* Vol.8, No.3, pp:211-224, Jun. 2004.

Liang Guo graduated from Shandong University and received Master's Degree in 2003. She graduated from Zhejiang University and received Doctor's Degree in 2006.

She is currently an Associate Professor with the Faculty of Mechanical Engineering & Automation, Zhejiang Sci-Tech University, Hangzhou, China. She was a Visiting Scholar with the Power Electronics and Machines Group, University Of Nottingham, UK. Her research interests include electromagnetic analysis and optimization of electrical machine, especially in permanent magnet machines.
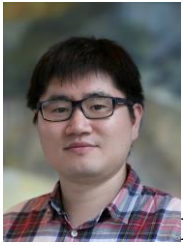
He Zhang (M'14) received his B.Eng. degree from Zhejiang University, China, in 2002. He obtained the Ph.D. degree in electrical machines from The University of Nottingham, UK, in 2009. Then he joined the UK Water Research Centre, and worked on energy efficiency determination for motor drive system for two years.

He is currently a senior research fellow and director of SNF machine drive technology centre within the Power electronics, Machines and Control research group in University Of Nottingham. His research interests include high performance electric machines and drives.

Michael Galea (M'14) received his PhD in electrical machines design from the University of Nottingham, UK, where he has also worked as a Research Fellow.

He is currently a Lecturer in Electrical Machines and Drives within the PEMC research group of the University of Nottingham. He is the Deputy Director of the Institute for Aerospace Technology at the University of Nottingham, where he is also a Lecturer in Aerospace Systems Integration. His main research interests are design, analysis and thermal management of electrical machines and drives.

Jing Li (M'15) received her MS.c (Distinction) and B.Eng. (Honour) from Beijing Institute of Technology, obtained the Ph.D degree from the University of Nottingham in 2010.

She is currently a research fellow in the Power electronics, Machine and Control group, University of Nottingham. Her research interests are condition monitoring for motor drive systems and power distribution systems, advanced control and design of motor drive systems.

Chris Gerada (SM'14) obtained his PhD in Numerical Modelling of Electrical Machines from the University of Nottingham, UK in 2005. He subsequently worked as a researcher at the University of Nottingham on high performance electrical drives and on the design and modelling of electromagnetic actuators for aerospace applications. He was appointed as Lecturer in Electrical Machines in 2008, an Associate Professor in 2011 and Professor in 2013.

His core research interests include the design and modelling of high performance electric drives and machines. Prof. Gerada holds a Royal Academy of Engineering / Cummins Chair in Electrical Machines. He is also an Associate Editor for the Transactions in Industry Applications and is the Chair of the IEEE Industrial Electronics society electrical machines technical committee.